Femtosecond measurement of shock wave driven twinning and lattice dynamics

Authors: C. E. Wehrenberg,[1*] D. McGonegle,[2] C. Bolme,[3] A. Higginbotham,[4] A. Lazicki,[1] H.J. Lee,[5] B. Nagler,[5] H.-S. Park,[1] B. A. Remington,[1] R. E. Rudd,[1] M. Sliwa,[2] M. Suggit,[2] D. Swift,[1] F. Tavella,[5] L. Zepeda-Ruiz,[1] and J.S. Wark[2]

Affiliations:

[1]*Lawrence Livermore National Laboratory, 7000 East Ave., Livermore CA 94550 USA.*

[2]*Department of Physics, Clarendon Laboratory, University of Oxford, Parks Road, Oxford, OX1 3PU, United Kingdom.*

[3]*Los Alamos National Laboratory, Bikini Atoll Road, SM-30, Los Alamos, NM 87545, USA*

[4]*University of York, Department of Physics, Heslington, York YO10 5DD, United Kingdom*

[5]*SLAC National Accelerator Laboratory, 2575 Sand Hill Rd, Menlo Park, CA 94025, USA*

*Correspondence to: wehrenberg1@llnl.gov

Understanding the deformation and associated defects created by shock waves is crucial in a wide range of fields, such as planetary formation and asteroid impact sites[1-3], formation of interstellar dust clouds[4], ballistic penetrators[5], spacecraft shielding[6], and ductility in high-performance ceramics[7]. Shock waves in solid materials can cause extreme damage and deformation. Twinning and dislocation-slip are the basic mechanisms of plastic deformation at the lattice level, yet diagnosing the active mechanism *in-situ* has been elusive. Methods for characterizing lattice defects have typically been limited to ex-post-facto experiments[8-11], which examine the microstructures of samples and are complicated by post-shock annealing[12] and reverberations. In addition measurements have been limited to relatively modest pressures. *In-situ* X-ray diffraction (XRD) experiments have provided new insights into dynamic material behavior[13] but are only starting to be applied to plasticity during shock compression[14-17], and have yet to provide detailed insight into competing deformation mechanisms. Here we present XRD experiments with femtosecond resolution that apply crystallographic techniques to capture *in-situ*, lattice-level pictures of the microstructural processes driving shock deformation. Tantalum, an important material for high-energy density physics applications, serves as a model body-centered cubic (BCC) material. For shock-compressed Ta, where simulations[18-20] and previous experiments[8-12] provide conflicting information on the dominant mechanism, we report twinning and related lattice rotation occurring on the time scale of tens of picoseconds. Despite a common association between twinning and strong shocks[21], we also find a transition from twinning to slip-dominated plasticity at high pressure (<150 GPa), a regime recovery experiments cannot accurately access. As the role of *in-situ* diffraction for studying shock waves and other high-rate phenomena continues to grow, the texture analysis techniques demonstrated here will be useful in studying a broad range of processes induced by plasticity.

40   Prior *in-situ* experimental measurements of lattice evolution during shock measurements
41   have not had sufficient time or spatial resolution to make critical direct comparisons to theory.
42   The need for a more direct comparison to theory is evident since, even for a well-studied BCC
43   metal such as Ta, existing experiments can disagree on the operative deformation mechanism,
44   twinning verse dislocation generation and transport (slip). Ta samples show significant twinning
45   at shock pressures above ~50 GPa[8-11], whereas previous *in-situ* diffraction experiments have not
46   registered a signal indicative of twinning at these pressures[16,17]. While the wide difference in
47   timescales makes comparing between experiments difficult, large-scale molecular dynamics
48   (MD) simulations in strongly shocked Ta also disagree. The deformation mechanism varies from
49   slip[18] to twinning[19] to a combination of the two mechanisms[20], depending on which interatomic
50   potential is used in the simulation. In this study the new capabilities offered by x-ray free-
51   electron laser sources are used to make direct comparisons to molecular dynamics simulations.

52   Here we use temporally resolved, *in-situ* x-ray diffraction to probe shocked polycrystalline
53   Ta, providing direct characterization of the mechanism and time scale of the ultrafast
54   deformation for shock pressures from 10 GPa to shock melt (~300 GPa). The experiments
55   were performed at the Matter in Extreme Conditions end station of the Linac Coherent
56   Light Source, and a sketch of the setup is shown in Figure 1. Probed during the initial
57   shock transit through the Ta, the diffraction patterns have signal from both driven and
58   undriven material. The material transitions rapidly to the shocked state. The low signal
59   level between driven and undriven lines implies a fast transition, occurring on timescales of
60   <100 ps for the highest pressures ($>10^9$ s^{-1} strain rate).

61   The Ta foil was fabricated by vapor deposition, which creates a fiber-like texture where
62   the grains share a common crystallographic direction along the sample normal ([110] in
63   this case) but are oriented randomly in the transverse direction. Having a known, highly-
64   textured starting material means new orientations created by deformation can be readily
65   observed in the diffraction data[22]. Twinning and slip produce distinct changes to the
66   texture of the Ta sample that can be used to determine the active mechanism for
67   deformation during shock compression. Both twinning and slip can cause a rotation of the
68   lattice when the sample is laterally confined during shock compression, since a lattice
69   rotation is needed to maintain the geometry of uniaxial compression[23]. However, twinning
70   also produces an additional mirror rotation in the twin grain.

71   Due to the highly-textured structure of the Ta foil, only certain spots are visible on
72   the powder Debye diffraction ring. The azimuthal positions of the spots correspond to the
73   angles of the respective diffraction planes. Figure 2 shows an example diffraction pattern
74   taken prior to shock loading. Contours of constant χ-angle, the angle between the
75   sample surface and the diffraction plane, are overlaid on the figure (constant 2θ is shown
76   with dashed lines). Two sketches of a Ta unit cell demonstrate that the {110} planes will
77   occupy angles of 60° or 90° relative to the sample plane. The {110} diffraction ring has
78   texture spots at corresponding χ of 60° and 90° (marked with green arrows). Similar
79   reasoning accounts for the azimuthal positions of texture spots for the other diffraction
80   rings.

81   Texture changes are evident in the driven data for a wide range of shock pressures, as
82   shown in the example diffraction patterns in Figure 3. Comparing χ for the compressed
83   and uncompressed spots reveals the texture change during shock compression. In Fig. 3a
84   (23 GPa), the d-spacing, the distance between lattice planes, decreases in the driven

85 portion of the sample and the diffraction lines move to higher 2θ angles, but no change in
86 χ is observed. At 46 GPa (Fig. 3b), a new set of spots forms on the compressed Debye
87 ring, marked with red arrows, that correspond to an orientation for twinning across a
88 {112} mirror plane (the dominant twin plane in BCC Ta). In the higher-pressure data (Fig
89 3c and d), the $\chi = 60°$ spot is elongated azimuthally; the texture spot spans the detector
90 gap in Fig. 3c and even splits into two spots (Fig. 3d). These changes in χ correspond to
91 lattice rotation, where the rotation moves some planes to higher χ and other planes to
92 lower χ. In contrast, no shift in χ is expected for the $\chi = 90°$ spot since the rotation occurs
93 in this plane.

94   The amount of texture change is plotted in Fig. 4a (twinning) and 4b (lattice rotation).
95 The twin fraction is minimal (consistent with zero) below 25 GPa, and increases with
96 shock pressure in the 25-75 GPa regime, reaching a twin fraction of ~30-40% at 75 GPa.
97 Surprisingly, even though twinning is often associated with strongly driven metals, at
98 higher shock pressures (>150-175 GPa), the twin fraction falls to low levels (< 10%). The
99 lattice rotation in Fig. 4b can be due to either slip or twinning and is found to increase
100 monotonically. Thus the decrease in twin fraction observed above ~150 GPa indicates a
101 transition to slip-dominated plasticity.

102   Figure 4c plots the equivalent plastic strain associated with twinning, γ_{Tw}^{P}, orange
103 triangles) and lattice rotation, γ_{Ro}^{P} (purple diamonds), while the plastic strain from slip can
104 be determined from the difference between γ_{Ro}^{P} and γ_{Tw}^{P}. The total strain for a given
105 shock is shown by γ_{Hu}^{P} (black line), the equivalent plastic strain on the Hugoniot. If either
106 mechanism dominates the response, the plastic strain from that mechanism will be a large
107 fraction of γ_{Hu}^{P}. While the onset of twinning occurs at 25 GPa, the plastic response is twin-
108 dominated in the 40-80 GPa range. Above 150 GPa, the plastic strain from twinning falls
109 well below the Hugoniot, indicating the plastic response becomes slip-dominated.

110   The trend for the lattice rotation follows the Hugoniot with a small offset. There is a
111 difference of 4% strain between the two curves, $\gamma_{Hu}^{P} - \gamma_{Ro}^{P} \sim 0.04$, indicated by the dashed
112 line in Fig 4c. In Fig. 4 b-d, the $\chi = 90°$ spots of the driven (110) Debye rings show
113 some azimuthal broadening. Since, as noted above, slip along {112} planes does not
114 affect the (110) $\chi = 90°$ planes, this broadening is an indication of a small amount of slip
115 along other planes and likely accounts for the 4% difference.

116   Phase transformations can also create texture changes and should be considered as a
117 possible response to shear strain[22]. While density functional theory indicates the BCC phase
118 is the stable phase for pressures up to 700 GPa and temperatures up to the melt line[24], the
119 plastic deformation of shock compression may drive a transition to the omega phase, as
120 indicated by recovery and MD simulations[2,25]. Our data does not show significant amounts
121 (>0.1%) of omega phase (see ED Fig. 1 & ED Fig. 2) or any other solid phase apart from
122 BCC for all pressures, from ambient up to melt at ~300 GPa.

123   We performed MD simulations using the Ravelo potential[26], simulating a Ta single crystal at
124 300 K shocked along the [110] direction. Figure 4a shows the simulated twin fraction and
125 Fig. 4b shows the simulated lattice rotation as a function of pressure (black circles). The
126 MD simulations show the onset of twinning occurring at similar pressures as the data,
127 although the decrease in twin fraction occurs at much lower pressure in the simulations.
128 The simulated lattice rotation is in good agreement with the data in the 75-200 GPa

129   pressure range.

130   The quantitative measurements provided by XRD allow direct comparison to simulations
131   and modeling. Complex constitutive models like the Livermore Multiscale Model[27] begin
132   with the assumption that plasticity is dislocation based. Even in the simplified case studied
133   here, where no phase transformations occur and loading is restricted to a single crystal axis,
134   the dominant deformation mechanism transitions multiple times, from minimal twinning to
135   twinning-dominated to slip-dominated, as the shock pressure is increased. Approaching
136   similar timescales to simulations and exploring high pressure regimes that are difficult to
137   observe and interpret in *ex-post-facto* experiments, these results highlight the importance
138   and growing role of *in-situ* experiments in studying materials in extreme conditions.

139

140

141

142

Fig. 1. Experimental configuration used at the MEC end station at LCLS for shock compression and *in-situ* x-ray diffraction. A shock wave is driven by laser ablation into a plastic ablator and Ta foil with a (110) fiber texture. The shock compressed Ta is probed by the LCLS beam and the resulting diffraction patterns are collected on an array of CSPADs.

148

Fig. 2. Example x-ray diffraction data from (110) fiber textured Ta prior to shock loading. A sketch of the diffraction geometry describes 2θ, the Bragg angle, and χ, the angle between the sample normal and diffraction plane normal. For a sample with (110) texture, {110} planes have $\chi=60°,90°$. The diffraction data have corresponding {110} texture spots at those χ angles, marked with green arrows. Solid curves indicate constant χ corresponding to specific lattice planes [for {110}: $\chi=60°,90°$; for {200}: $\chi=90°, 45°$; for {211}: $\chi=73°, 54.7°$]. The dashed curves indicate constant 2θ.

156

Fig. 3. Diffraction patterns from Ta shock compressed at (a) 19, (b) 44, (c) 108, and (d) 169 GPa. The driven spots appear at higher diffraction angle, which appears as a shift upwards in this view. Lines of constant χ -angle are shown at 60° and 90° to illustrate the reorientation of the texture spots in the driven Ta. At 23 GPa (a) no reorientation is observed, since the driven and undriven diffraction spots have the same azimuthal location. At 46 GPa, new texture spots arise corresponding to twinning across a {112} mirror plane plus an additional 2.5° rotation. At higher pressures, (c) and (d), large lattice rotations are observed, causing the $\chi=60°$ (110) spot (marked with red arrows) to elongate and then split.

166

Fig. 4. Twin fraction, rotation and plastic strain computed from the diffraction data. (a) Twin fraction as a function of shock pressure measured by the ratio of texture spots (orange triangles) and from MD simulations (black circles). (b) Lattice rotation angle from XRD (purple diamonds) and from MD simulations (black circles). (c) Equivalent plastic strain inferred from lattice rotation (purple diamonds) and twin fraction (orange triangles). The equivalent plastic strain on the Hugoniot is plotted (black line). The rotation data follows the Hugoniot line minus 4% strain (dotted line). Twinning accounts for the majority of the Hugoniot plastic strain in the 40-80 GPa range (pink shaded region is a guide to the eye), but falls well below the Hugoniot above 150 GPa (blue shaded region), indicating the response is slip dominated.

177

References:
1. Ashworth, J. R. & Schneider, H. Deformation and Transformation in Experimentally Shock-Loaded Quartz. *Phys. Chem. Minerals.* **11**, 241 (1985).

181

182 2. French, B. & Koeberl, C. The convincing identification of terrestrial meteorite impact
183 structures: What works, what doesn't, and why. *Earth Sci. Rev.* **98**, 123-170 (2010).

184

185 3. Gattacceca, J., Lamali, A., Rochette. P., Boustie, M. & Berthe, L. The effects of explosive-
186 driven shocks on the natural remanent magnetization and the magnetic properties of rocks. *Phys.*
187 *Earth and Planet. Inter.* **162**, 85-98 (2007).

188

189 4. Draine, B. T. & Salpeter. E. E. Destruction mechanisms for interstellar dust. *Astrophys. J.* **231**,
190 438-455 (1979).

191

192 5. Pappu, S., Kennedy, C., Murr, L. E., Magness, L. S. & Kapoor, D. Microstructure analysis and
193 comparison of tungsten alloy rod and [001] oriented columnar-grained tungsten rod ballistic
194 penetrators. *Mat. Sci. & Eng. A*. **262**, 115-128 (1999).

195

196 6. Thoma, K., Schafer, F., Hiermaier, S. & Schneider, E. An approach to achieve progress in
197 spacecraft shielding. *Adv. Space Res.* **34**, 1063-1075 (2004).

198

199 7. Chen, M. W., McCauley, J. W., Dandekar, D. P. & Bourne, N. K. Dynamic plasticity and
200 failure of high-purity alumina under shock compression. *Nature Mater.* **5**, 614-618 (2006).

201

202 8. Murr, L.E. *et al.* Shock-induced deformation twinning in tantalum. *Acta Mat.* **45**, 157-175
203 (1996).

204

205 9. Hsiung, L. L. & Lassila, D. H. Shock-induced deformation twinning and omega
206 transformation in tantalum and tantalum-tungsten alloys. *Act. Mat.* **48**, 4851-4865 (2000).

207

208 10. Lu, C. H. *et al.* Laser compression of monocrystalline tantalum. *Acta Mat.* **60**, 6601-
209 6620 (2012).

210

211 11. Florando, J. N., Barton, N. R., El-Dasher, B. S., McNaney, J. M. & Kumar, M. Analysis
212 of deformation twinning in tantalum single crystals under shock loading conditions. *J. Appl.*
213 *Phys.* **113**, 083522 (2013).

214

215 12. Lu, C. H. *et al.* Laser compression of nanocrystalline tantalum. *Acta Mat.* **61**, 7767-7780
216 (2013).

217

218 13. Loveridge-Smith, A. *et al.* Anomalous elastic response of silicon to uniaxial shock
219 compression on nanosecond time scales. *Phys. Rev. Lett.* **86**, 2349-2352 (2001).

220

221 14. Suggit, M. J. et al. Nanosecond white-light Laue diffraction measurements of dislocation
222 microstructure in shock-compressed single-crystal copper. *Nature Comm.* **3**, 1224 (2012).

223

224 15. Milathianaki, D. *et al.* Femtosecond visualization of lattice dynamics in shock-
225 compressed matter. *Science* **342**, 220-223 (2013).

226

227   16. Comley, A. J. *et al.* Strength of shock-loaded single-crystal tantalum [100] determined
228   using *in-situ* broadband *Phys. Rev. Lett*. **110**, 115501 (2013).
229
230   17. Wehrenberg, C. E. *et al.* Lattice-level observation of the elastic-to-plastic relaxation
231   process with subnanosecond resolution in shock-compressed Ta using time-resolved in situ
232   Laue diffraction. *Phys. Rev. B* **92**, 104305 (2015).
233
234   18. Rudd, R. E. *et al.* Theory and simulation of 1D to 3D plastic relaxation in tantalum. *AIP*
235   *Conf. Proc.* **1426**, 1379 (2012).
236
237   19. Higginbotham, A. *et al.* Molecular dynamics simulations of shock-induced deformation
238   twinning of a body-centered-cubic metal. *Phys. Rev. B* **88**, 104105 (2013).
239
240   20. Tramontina, D. *et al.* Molecular dynamics simulations of shock-induced plasticity in
241   tantalum. *High Energy Den. Phys*. **10**, 9 (2014).
242
243   21. Meyers, M. "Plastic deformation in shock waves" in *Dynamic Behavior of Materials*
244   (John Wiley and Sons, Inc., New York, 1994).
245
246   22. McGonegle, D., Milathianaki, D., Remington, B. A., Wark, J. S. & Higginbotham, A.,
247   Simulations of in situ X-ray diffraction from uniaxially compressed highly textured
248   polycrystalline targets. *J. Appl. Phys.* **118**, 065902 (2015).
249
250   23. Fleischer, R. L. Single crystal lattice rotation during compression. *J. Mech. Phys. Solids*
251   **6**, 301-306 (1958).
252
253   24. Miljacic, L., Demers, S., Hong, Q.-J. & van de Walle, A. Equation of state of solid, liquid
254   and gaseous tantalum from first principles. *CALPHAD* **51**, 133-143 (2015).
255
256   25. Lu, C. H., Hahn, E. N., Remington, B. A., Maddox, B. R. & Meyers, M. A. Phase
257   transformation in tantalum under extreme laser deformation. *Sci. Rep*. **5**, 15064 (2015).
258
259
260   26. Ravelo, R., Germann, T. C., Guerrero, O., An, Q. & Holian, B. L. Shock-induced
261   plasticity in tantalum single-crystal: Interatomic potentials and large-scale molecular-
262   dynamics simulations. *Phys. Rev. B* **88**, 134101 (2013).
263
264   27. Barton, N. R. *et al.* A multiscale strength model for extreme loading conditions. *J. Appl.*
265   *Phys*. **109**, 073501 (2011).
266

279
280 **Author contributions:** The experiments were conceived by C.E.W., D. M., B.A.R., A. H.,
281 M.J.S., R.E.R. and J.S.W., and were performed by C.E.W., D. M., B.A.R., A. H., J.S.W.,
282 H.-S.P, D.S., A.L., C. B., H.J.L., B. N., and F. T. The data were analyzed by C.E.W., D.
283 M., A.L. and M.S. and the results were interpreted by C.E.W., D.M., M.J.S., A. H., B.A.R.,
284 J.S.W., and R.E.R. Molecular dynamics simulations were performed by D.M., A.H., L.Z.-
285 R., and R.E.R. The manuscript was written by C.W., B.A.R, R.E.R, J.S.W., and D.M.

Methods

290

291   The experiments were performed at the Matter in Extreme Conditions (MEC) end station of
292 the Linac Coherent Light Source (LCLS). The Ta structure was probed while under shock
293 compression and the resulting diffraction patterns were recorded on several Cornell-SLAC
294 hybrid Pixel Array Detectors (CSPADs)[27], as shown in Fig. 1. A planar shock was driven by
295 direct laser ablation from frequency doubled (527 nm) laser beams, using a 5-10 ns square pulse.
296 Hybrid phase plates were used to modify the focal spot. These plates use surface features to shift
297 the phase of the light, creating focal spots of 100 μm, 150 μm or 250 μm diameter with "top-hat"
298 intensity profiles. Each target consisted of a 50 μm thick kapton ablator glued to a 6 μm thick
299 foil of Ta. The ablator thickness (several times larger than the sample) prevents reverberations
300 from entering the Ta before the initial shock has passed through the sample. The thickness of the
301 ablator also helps to smooth out spatial variations in drive created by speckle pattern of the laser
302 spot. The Ta foil was fabricated by vapor deposition onto a SiO_2 substrate at a temperature
303 (~450°C) sufficient both to create the body-centered cubic (BCC) α-Ta phase and to delaminate
304 the Ta from the substrate upon cooling. Small amounts (<0.5%) of β phase are also present in
305 some of the Ta samples.

306   A Velocity Interferometer System for Any Reflector (VISAR) diagnostic was used to
307 monitor the free surface velocity of the Ta during the shock compression and release and
308 help set the diffraction timing. The optical streak camera system (line VISAR) was used to
309 confirm the planarity of the drive. The VISAR images show the planar driven region
310 approximately corresponds to the size of the phase plates, and this planar region larger than the
311 20-μm x-ray beam. An example of the VISAR data for a 130 GPa shock is shown in ED Fig 3.

312   The LCLS x-ray beam was tuned for 9.6 keV photons in a 50 fs pulse. The diffraction angles
313 were calibrated using a powder sample of LaB_6 and CeO_2 standards. The calibrated detector
314 positions were then used to measure the diffraction angles from the Ta samples. The sample
315 orientation is determined by fitting the χ of the spots of the ambient diffraction pattern. The
316 amount of lattice rotation can then be determined from the χ of the driven spots. A single
317 rotation from the original [110] orientation is determined that best fits the measured χ of the
318 driven spots. The diffracted intensity was adjusted to account for polarization of the x-ray beam
319 using the following factor:

320 $$P = (\cos^2\phi * \cos 2\theta)^2 + \sin^2\phi \qquad\qquad P = [\cos^2\phi * \cos(2\theta)]^2 + \sin^2\phi$$

321 where ϕ is the azimuthal angle for diffracted x-rays. The pressure produced by the shock loading
322 was calculated from the d-spacing measured by diffraction assuming BCC structure.
323 Specifically, the shock pressure was found using the shock speed data from Mitchell and
324 Nellis[28], $U_S = C_0 + S*U_p$ where $C_0 = 3293$ m/s and S=1.307, which together with the Rankine-
325 Hugoniot equations, give the following expression for the shock pressure[29]:

326 $$P_x = \rho_0 C_0^2 \frac{1-(d/d_0)^3}{1-S[1-(d/d_0)^3]} \qquad\qquad P_x = \rho_0 C_0^2(1-[d/d_0]^3)/(1-S[1-(d/d_0)^3])$$

327 where ρ is the initial density and d_0 and d are the initial and compressed lattice spacings. Since
328 the error in determining the peak positions in the diffraction data is small, the main sources of
329 uncertainty in determining the pressure are the spatial and temporal non-uniformity in the drive.
330 These non-uniformities will not significantly change the average pressure, but may affect the
331 range of pressures present in the sample. The VISAR records show that the drive is steady prior

332 to the first reverberation. Some spatial non-uniformity is present but is small over the 20 μm
333 region probed by the x-ray beam. Based on uncertainty in fitting the peak positions, the pressure
334 uncertainty is +/- 3 GPa.

335   For high pressure shots, where the driven diffraction pattern had the diffuse signal indicative
336 of a liquid sample, the pressure could not be reliably measured from the diffraction data. The
337 pressure estimate from the laser ablation intensity is consistent with previous measurements of
338 the shock melting pressure, ~300 GPa[30].

339
340 **Expected signal if omega phase (ω) were present**
341   We have analyzed the diffraction data for the presence of omega (ω) phase. This phase has
342 been observed in shock-recovered Ta samples by Hsiung and Lassila[2] and Lu et al.[25]. Hsiung
343 provides the following relationship between the BCC and hexagonal lattice parameters:

344 $$a_\omega = \sqrt{2}a_\alpha, c_\omega = \frac{\sqrt{3}}{2}a_\alpha \qquad\qquad a_\omega = \sqrt{2}a_\alpha , c_\omega = \sqrt{3}/2a_\alpha$$

345 where a_α is the lattice parameter of the BCC phase, and c_ω and a_ω correspond to the omega
346 phase. Lu et al. were able to match their TEM diffraction pattern using these lattice parameters.
347 Lu et al. reported observing ω phase in samples that are recovered following shock loading to
348 ~70 GPa. In ED Fig 1. we show our driven data for a 73 GPa shock and indicate the expected
349 peak positions for the hexagonal structure as well as the "rumpled" hexagonal structure reported
350 by Hsiung and Lassila.
351   Since the initial ta structure is highly textured, the transformed omega phase may also be
352 highly textured. Lu et al. state that they observed the same orientation relationship between the
353 matrix and omega phase as Hsiung and Lassila, namely that the $(111)_m$ // $(0001)_\omega$ and $[110]_m$ //
354 $[1000]_\omega$ where m refers to the matrix BCC phase and ω is the transformed omega phase.
355 Using this relationship, we show in ED Fig. 2. the azimuthal positions of the texture spots for the
356 omega phase (white lines). For simplicity, the rumpled structure is not shown. The detectors
357 cover multiple spots where the omega peaks would be expected given the previously reported
358 orientation relationships yet no signal was observed.

359
360 **Twin fraction calculation**
361   We have measured the twin fraction by comparing the intensity of texture spots
362 corresponding to the twin orientation with the intensity of other driven and undriven texture
363 spots.   In addition, the differing multiplicities of various planes associated with specific χ must
364 be considered. For example, a unit cell in the twin orientation will have twice as many planes for
365 $\chi = 90°$ than $\chi = 70.5°$, so that the twin fraction is given by,

366 $$f_{Tw} = \frac{2 * I_{Drvn(110)\chi=70.5}}{I_{Drvn(110)\chi=90}} \qquad\qquad f_{Tw} = (2 * I_{Drvn(110)\chi=70.5})/(I_{Drvn(110)\chi=90})$$

367 where I refers to the integrated intensity of the specified diffraction spot. This equation assumes
368 azimuthal symmetry, since the two spots being compared have different azimuthal positions.
369 The azimuthal variation of the (110) fiber texture was not known prior to the experiments, so the
370 variation is a source of uncertainty in our measurements. Pole figure measurements were
371 performed on remaining samples, and azimuthal lineouts, normalized relative to the azimuthal
372 average, follow a roughly sinusoidal pattern with 180° rotational symmetry and variation in
373 intensity of +/- 30%.

374   Similar calculations were performed for the (200) $\chi=76.3°$ and (211) $\chi=61.3°$ twin spots, and
375 the results were averaged to arrive at the final twin fraction values. The error bars were set to the
376 standard deviation of the measurements using the three lines. For shock pressures in the 50-150
377 GPa range, some of the driven twin spots fall into gaps between the detectors, limiting
378 measurements in this pressure regime. The error was assumed to be 50% when twin spots were
379 measured on only one diffraction line, which reflects the uncertainty in the azimuthal texture in
380 both the twin spot and the reference spot.

381   We can quantitatively determine the role of twinning in the overall plastic response by
382 comparing the plastic strain from twinning, $\gamma_{Tw}{}^{P}$, to the total plastic strain imparted by the
383 shock, $\gamma_{Hu}{}^{P}$. Eqs. (1) and (2) give the two plastic strain quantities:

384 $$\gamma_{Tw}^{p} = f_{Tw} * \varepsilon_0 * M \qquad\qquad \gamma_{Tw}{}^{P} = f_{Tw} * \varepsilon_0 * M \qquad\qquad (1)$$

385 $$\gamma_{Hu}^{p} = 2/3\ln\left(\frac{V_0}{V}\right) \qquad\qquad \gamma_{Hu}{}^{P} = 2/3\ln(V_0/V) \qquad\qquad (2)$$

386   where f_{Tw} is the twin fraction, ε_0 is the eigenstrain, and M is the Schmid factor (for
387 [110] loading, $\varepsilon_0 = 0.707$ and $M = 0.471$), and V_0 and V are the specific volumes in the
388 ambient and shocked conditions respectively[31,21]. We have taken the residual elastic shear
389 strain to be negligible due to the absence of diffraction ring distortion (discussed below),
390 implying full plastic relaxation of the shear stress on the ultrashort time scale of the
391 experiment.

392   The {112} planes serves as the dominant plane for both slip and twinning, meaning both
393 mechanisms will produce similar lattice rotations. The observed rotation, found by fitting
394 the azimuthal position of the diffraction spots, provides a measurement of the plastic strain
395 caused by both mechanisms, γ_{Ro}^{p}, as shown by Eq (3),

396 $$\gamma_{Ro}^{p} = \ln\left(\frac{\cos\chi}{\cos\chi_0}\right) \qquad\qquad \gamma_{Ro}{}^{P} = \ln(\cos\chi/\cos\chi_0) \qquad\qquad (3)$$

397 where χ_0 and χ correspond to the initial and final angles between the slip plane normal
398 and the compression direction.
399
400 ## How the plastic strain is calculated as a function of rotation
401
402   Here we discuss the relation between the plastic strain and the rotation that is measured.
403 Throughout this analysis we assume that the residual shear stress in the shocked Ta is zero or so
404 small that it can be neglected. This assumption, justified by the ring distortion analysis in the
405 next section, allows us to impose that the elastic strain in the shocked state is strictly hydrostatic.

406 $$\varepsilon_x^e + \varepsilon_y^e + \varepsilon_z^e = \ln\left(\frac{V}{V_0}\right) \qquad\qquad \varepsilon_x{}^e + \varepsilon_y{}^e + \varepsilon_z{}^e = \ln(V/V_0)$$

407 $$\varepsilon_x^e = \varepsilon_y^e = \varepsilon_z^e = 1/3\ln\left(\frac{V}{V_0}\right) \qquad\qquad \varepsilon_x{}^e = \varepsilon_y{}^e = \varepsilon_z{}^e = 1/3\ln(V/V_0)$$

408 where ε_x^e is the elastic strain in the shock direction and ϵ_y^e and ϵ_z^e are the transverse elastic
409 strains. Similarly, we assume the plastic strains do not change the volume

| 410 | $$\varepsilon_x^p + \varepsilon_y^p + \varepsilon_z^p = 0$$ | $\varepsilon_x{}^p + \varepsilon_y{}^p + \varepsilon_z{}^P = 0$ |

411 That uniaxial compression of crystals produces a rotation of the lattice is well known, and the
412 rotation as function of compression is[23]

| 413 | $$\varepsilon_x^p = \ln\left(\frac{\cos\chi_0}{\cos\chi}\right)$$ | $\varepsilon_x{}^p = \ln(\cos\chi/\cos\chi_0)$ |

414 where χ and χ_0 give the angle between the slip plane normal and the compression direction and
415 ϵ_x^p is the plastic strain along the compression direction.

416   Since the material is laterally constrained and compressed along the high symmetry [110]
417 direction, we assume that, while individual grains may expand or contract in different transverse
418 directions, the area of each grain transverse to the sample normal will remain the same. Thus we
419 find that the total strain in the two transverse directions remains the same:

| 420 | $$\varepsilon_y^e + \varepsilon_y^p + \varepsilon_z^e + \varepsilon_z^p = 0$$ | $\varepsilon_y{}^e + \varepsilon_y{}^p + \varepsilon_z{}^e + \varepsilon_z{}^P = 0$ |

421

| 422 | $$\varepsilon_x^p = \varepsilon_y^e + \varepsilon_y^e = \frac{2}{3}\ln\left(\frac{V}{V_0}\right)$$ | $\varepsilon_x{}^P = \varepsilon_y{}^e + \varepsilon_y{}^e = 2/3\ln(V/V_0)$ |

423 therefore

| 424 | $$\frac{\cos\chi_0}{\cos\chi} = \left(\frac{V}{V_0}\right)^{2/3}$$ | $\cos\chi_0/\cos\chi = (V/V_0)^{2/3}$ |

| 425 | $$\gamma_p = -\frac{2}{3}\ln\left(\frac{V}{V_0}\right) = \ln\frac{\cos\chi}{\cos\chi_0}$$ | $\gamma_p = -2/3\ln(V/V_0) = \ln(\cos\chi/\cos\chi_0)$ |

426
427 For the (211) slip plane, $\chi_0 = 54.7$
428
429 **Residual Elastic Shear Stress**
430   We have analyzed the Debye rings for deviations from circularity that would indicate shear
431 stress in the shocked state. When using the Hugoniot jump conditions to calculated the pressure
432 from the measured d-spacing, or when calculating the equivalent plastic strain, we have assumed
433 that the residual elastic shear stress is near zero. Residual elastic shear strain would mean that the
434 strain is anisotropic, with higher elastic strain in the compression direction (shock prorogation
435 direction) and less in the transverse direction. This anisotropic elastic strain would manifest as a
436 Debye-ring distorted by varying d-spacing, making it appear elliptical[32]. With no shear strain, the
437 Debye-ring has constant 2θ. As shear strain increases, the driven rings move to higher 2θ for
438 low χ (right side of the diffraction pattern) and to lower 2θ for high χ (left side of the diffraction
439 pattern). While 0% strain produces a good fit to the data, small shear strains may also match.

440 We find at 2-3% shear strain, the data no longer provides a good match. Thus the assumption
441 that the elastic shear strain is negligible is likely valid.
442
443 **Molecular Dynamics Simulations**
444 Molecular dynamics simulations were performed using the LAMMPS code[33] and the Ravelo
445 potential[26] for 100x100x800 unit cells (330x330x2644 Å). A portion of the end of sample is used
446 as a piston. That section is "frozen" so that it won't respond to external forces and then ramped
447 up to a set velocity to drive the shock. By performing a 3D Fourier Transform[34] of the
448 plastically deformed region behind the shock front, we can find the average rotation of the
449 crystal lattice about the [1-10] axis. The Per Atom Structure Factor (PASF) code[12] was used to
450 determine the twin fraction in the same region.
451
452 **Data Availability.** The datasets generated and analyzed during the current study are available
453 from the authors on reasonable request.
454
455
456 27. Philipp, H. T., Hromalik, M., Tate, M., Koemer, L. & Gruner, S. M. Pixel array detector
457 for X-ray free electron laser experiments. *Nucl. Instrum. Methods Phys. Res. A* **649**, 67
458 (2011).
459
460 28. Mitchell, A. C. & Nellis, W. J. Shock compression of aluminum, copper and tantalum. *J.*
461 *Appl. Phys.* **52**, 3363 (1981).
462
463 29. Meyers, M. "Shock Waves: Equations of State" in *Dynamic Behavior of Materials* (John
464 Wiley and Sons, Inc., New York, 1994).
465
466 30. Brown, J. M. & Shaner J. W. in *Shock Waves in Condensed Matter*—1983, ed. J. R. Asay et
467 al. (Elsevier, New York, 1984), p. 91.
468
469 31. Kalidindi, S. R. Incorporation of deformation twinning in crystal plasticity models. *J.*
470 *Mech. Phys. Solids.* **46**, 267-290 (1998).
471
472 32. Higginbotham, A. & McGonegle, D. Prediction of Debye-Scherrer diffraction patterns
473 in arbitrarily strained samples. *J Appl Phys.* **115**, 174906 (2014).
474
475 33. Plimpton, S. Fast parallel algorithms for short-range molecular dynamics. *J. Comput. Phys.*
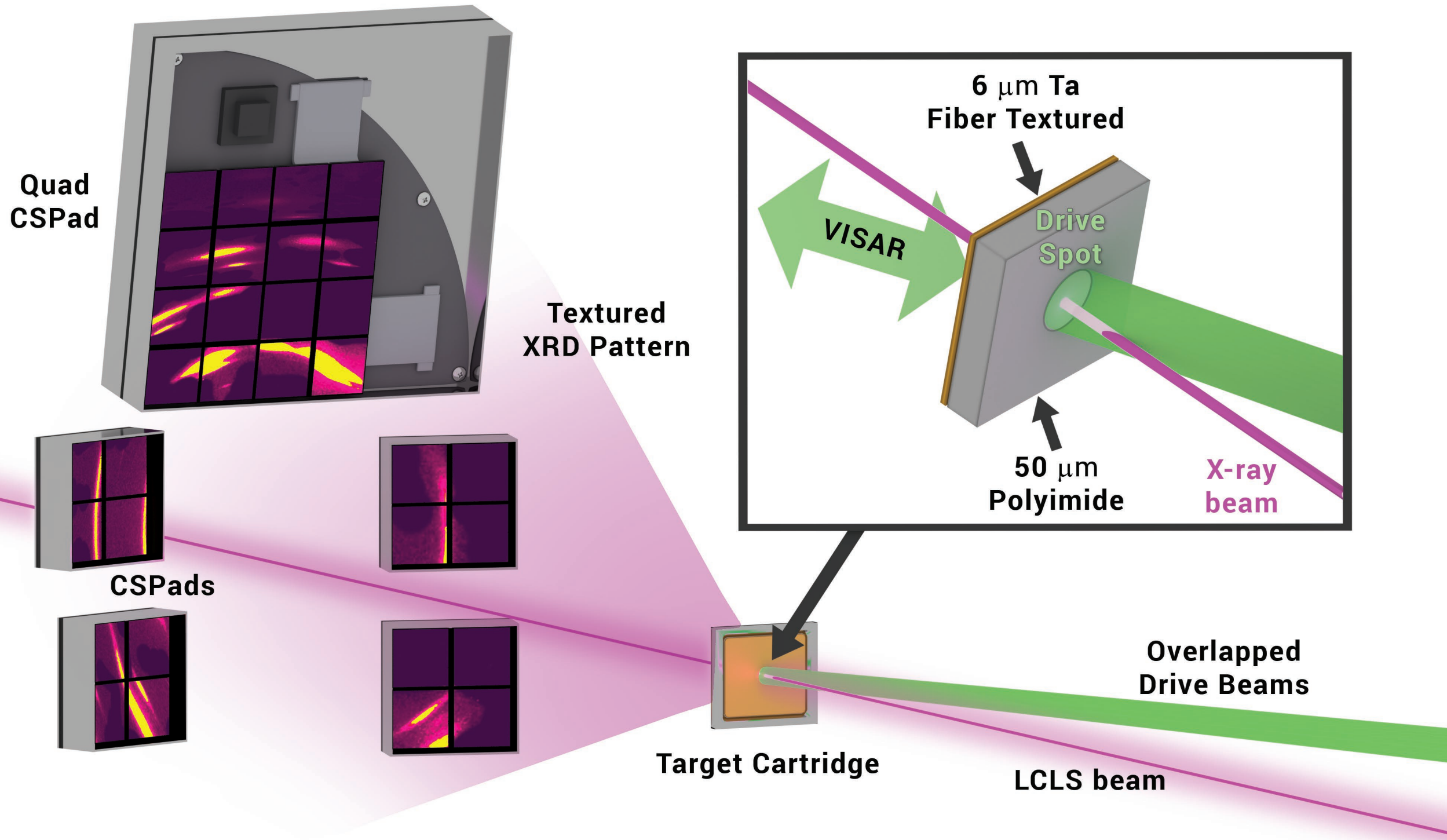476 **117**, 1-19 (1995).
477
478 34. Kimminau, G. *et al.* Simulating picosecond x-ray diffraction from shocked crystals using
479 post-processing molecular dynamics calculations. *J. Phys.: Condens. Matter* **20**, 505203 (2008).
480
481

482

483

484

485 ED Fig. 1. Diffraction angle (2θ) plotted vs. x-ray counts averaged over 2π in azimuthal
486 angle for a shock pressure of 73 GPa. The indices of the ambient pattern, matching BCC
487 with lattice parameter of a=3.308 Å, are marked in green. The driven pattern (black dots)
488 match BCC with a=3.051 Å. Indexed peak positions for the hexagonal phase are marked with
489 red lines, and peaks corresponding to the "rumpled" structure observed by Hsiung & Lasilla[2]
490 are marked with an asterisk. Both BCC and omega phase overlap the observed peaks, but
491 additional peaks are expected for the omega phase that are not observed.

492 ED Fig. 2. Diffraction pattern for 73 GPa shock showing raw data (left) and overplotted with
493 BCC and omega phase (right). The ambient BCC phase is marked with blue. Compressed and
494 rotated BCC phase is marked in black, and the expected positions of the omega phase are marked
495 in white.
496

497 ED Fig. 3. Example VISAR streak image for a 130 GPa shot using a 250 μm phase plate. The
498 planar region of the shock, roughly similar in dimensions to the phase plate size, breaks out of
499 the Ta free surface at 7.4 ns. The x-ray beam probes a 20 μm region in the center of the planar
500 shock.

501

502

503

Quad CSPad

Textured XRD Pattern

CSPads

6 μm Ta Fiber Textured

VISAR

Drive Spot

50 μm Polyimide

X-ray beam

Target Cartridge
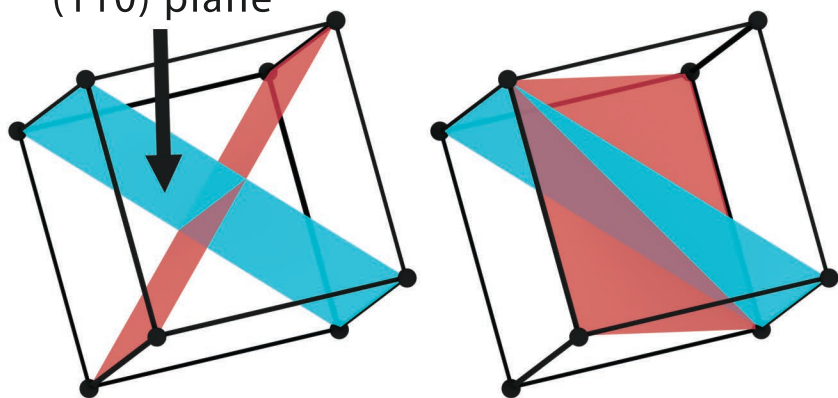
Overlapped Drive Beams

LCLS beam

Sample Normal

C

Plane Normal

2q

(110) Texture

Sample ∥ to (110) plane

C=90°   C=60°

Constant C-angle

{220} 2q=66.8°

C=90°

{211} 56.9°

{200} 45.9°

{110} 32.0°

73°   60°   54.7°

90°   60°

45°

90°

(a) 23 GPa 60°

(200)

Driven

90°

(110)

Undriven

(b) 46 GPa

Twin Spots

(c) 108 GPa

Broadening from Rotation

(d) 169 GPa

Peak Splitting from Rotation

a

Twin Fraction

▲ Diffraction Data
● MD Simulation

b

Rotation Angle (deg)

◆ Diffraction Data
● MD Simulation

c

Hugoniot

Twin Dominated

Equiv Plastic Strain

Slip Dominated

−0.04

Pressure (GPa)

0